From prediction to experimental realization of ferroelectric wurtzite $Al_{1-x}Gd_xN$ alloys

Cite as: APL Mater. 13, 021114 (2025); doi: 10.1063/5.0251168
Submitted: 29 November 2024 • Accepted: 4 February 2025 •
Published Online: 21 February 2025

Cheng-Wei Lee,[1] Rebecca W. Smaha,[2] Geoff L. Brennecka,[1] Nancy M. Haegel,[2] Prashun Gorai,[1,2,3,a)] and Keisuke Yazawa[1,2,b)]

AFFILIATIONS

[1] Colorado School of Mines, Golden, Colorado 80401, USA
[2] National Renewable Energy Laboratory, Golden, Colorado 80401, USA
[3] Rensselaer Polytechnic Institute, Troy, New York 12180, USA

Note: This paper is part of the Joint Special Topic on Energy-Efficient Memory Materials from APL Materials and APL Energy.
[a)] **Electronic mail:** goraip@rpi.edu
[b)] **Author to whom correspondence should be addressed:** Keisuke.Yazawa@nrel.gov

ABSTRACT

AlN-based alloys find widespread application in high-power microelectronics, optoelectronics, and electromechanics. The realization of ferroelectricity in wurtzite AlN-based heterostructural alloys has opened up the possibility of directly integrating ferroelectrics with conventional microelectronics based on tetrahedral semiconductors, such as Si, SiC, and III–Vs, enabling compute-in-memory architectures, high-density data storage, and more. The discovery of AlN-based wurtzite ferroelectrics has been driven to date by chemical intuition and empirical explorations. Here, we demonstrate the computationally-guided discovery and experimental demonstration of new ferroelectric wurtzite $Al_{1-x}Gd_xN$ alloys. First-principles calculations indicate that the minimum energy pathway for switching changes from a collective to an individual switching process with a lower overall energy barrier, at a rare-earth fraction x with $x > 0.10$–0.15. Experimentally, ferroelectric switching is observed at room temperature in $Al_{1-x}Gd_xN$ films with $x > 0.12$, which strongly supports the switching mechanisms in wurtzite ferroelectrics proposed previously [Lee *et al.*, Sci. Adv. **10**, eadl0848 (2024)]. This is also the first demonstration of ferroelectricity in an AlN-based alloy with a magnetic rare-earth element, which could pave the way for additional functionalities such as multiferroicity and opto-ferroelectricity in this exciting class of AlN-based materials.

I. INTRODUCTION

Ferroelectric (FE) materials are potentially useful for energy-efficient computing architectures, including compute-in-memory, neuromorphic computing, and high-density non-volatile memory, among other circuit components.[1,2] Wurtzite nitride ferroelectrics are of particular interest due to their chemical, structural, and process compatibility with commercial semiconductors, such as Si, SiC, and GaN, all of which exhibit tetrahedron-based crystal structures.[3] In addition, the relatively low deposition temperatures (<400 °C) required for growth of wurtzite nitrides make them compatible with back end of line (BEOL) semiconductor manufacturing processes if full integration is not necessary. Wurtzite nitrides are also generally resistant to anion migration,[4,5] which is responsible for fatigue and aging in common oxide ferroelectrics, such as $Pb(Zr_xTi_{1-x})O_3$ (PZT) and HfO_2.[6,7] Here, and subsequently, the term "wurtzite" also includes wurtzite-derived structures.[8]

However, there are challenges in employing wurtzite nitride FEs in practical applications. The electric field required to switch polarization, i.e., the coercive field (E_c), is typically a few MV/cm, which is close to the breakdown field (E_B) of all known wurtzite ferroelectrics. Such large E_c requires FE thin films with thicknesses on the order of nanometers to meet the operating voltage specifications of 1–2 V (or less) in conventional microelectronics. With such aggressive scaling, interfaces and their associated defects become increasingly dominant, which means that successful scaling in this case would require the coercive voltage to decrease with thickness faster than any associated increase in detrimental characteristics such as leakage and trap states. Lowering E_c and controlling bulk and interfacial defects remain major challenges for wurtzite FEs.[9] Since

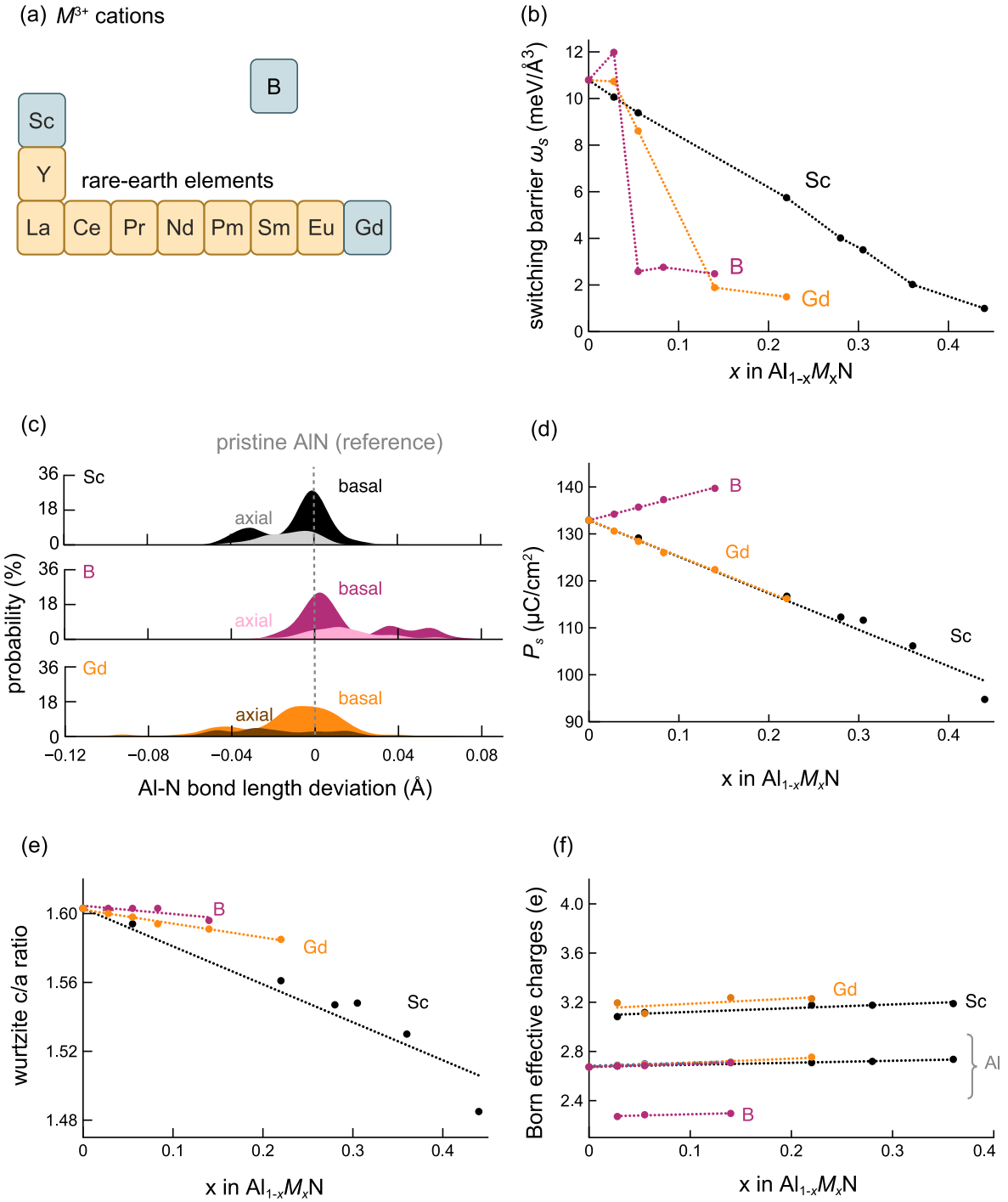

FIG. 1. Ferroelectric and structural characteristics of $Al_{1-x}M_xN$ alloys (M = B, Sc, and Gd). The data for $Al_{1-x}Sc_xN$ are taken from Ref. 21. (a) M^{3+} cations that form MN nitrides in non-wurtzite ground-state structures. The alloys of AlN with elements in blue are examined in this study. (b) Calculated polarization switching barrier as a function of alloy composition. (c) Deviation in Al–N bond lengths in $Al_{0.945}M_{0.055}N$ relative to pristine AlN, categorized into basal and axial Al–N bonds. (d) Spontaneous polarization as a function of alloy composition. (e) Wurtzite c/a ratio as a function of alloy composition. (f) Born effective charges in the polar c-axis direction. The standard deviations can be found in Figs. S2 and S5.

the initial demonstration of polarization switching in $Al_{1-x}Sc_xN$ in 2019, efforts have primarily focused on E_c reduction through strain engineering.[10–14] While in-plane biaxial tensile strain can reduce E_c, it is not as effective as in oxide perovskite FEs.[15] First-principles calculations suggest that E_c can be modestly reduced by certain defects in nitrides, including native vacancies and oxygen impurities, but these studies await experimental verification.[9]

An alternative approach is to discover and/or develop new materials with lower E_c.[16–19] Recent experimental and theoretical efforts have focused on heterostructural alloying of AlN and GaN with various nitrides of M^{3+} cations, e.g., M = B, Sc, and Y [Fig. 1(a)]. Ferroelectricity has been reported in various nitride alloys, including $Al_{1-x}B_xN$,[12] $Ga_{1-x}Sc_xN$,[11] and $Al_{1-x}Y_xN$,[20] with E_c of similar order. Computationally-guided searches have identified additional candidates for ferroelectricity,[17–19] but most still await experimental confirmation.

In principle, other AlN alloys (in fact, any polar material for which $E_c < E_B$) should also exhibit ferroelectricity. We are particularly interested in rare-earth M^{3+} elements because of their chemical similarity to Sc and Y. In addition, successful demonstration of FE polarization switching with rare-earth M^{3+} cations will open up opportunities to introduce additional functionalities, such as optical emission, multiferroicity, and/or other phenomena in wurtzite nitrides, although this is beyond the scope of the current study.

In this work, we demonstrate the computationally-guided discovery of new FE wurtzite $Al_{1-x}Gd_xN$ alloys. Our prior work suggested that the key mechanism by which Sc additions reduce E_c of $Al_{1-x}Sc_xN$ alloys is by disrupting the nearby Al–N bonds,[14] so we chose to study large ions that should be effective in disrupting the Al–N network with more ionic bonding. We employ first-principles density functional theory calculations in conjunction with the modern theory of polarization and solid state-nudged elastic band (SS-NEB) method to predict that polarization switching can be achieved in alloy compositions of x above 0.10–0.15. We show that the switching barrier, which is related to E_c, is reduced when the switching mechanism changes from collective to individual.[21] For wurtzite materials, previously predicted minimum energy paths between positively and negatively polarized structures show that the cation-centered tetrahedra within a unit cell can flip their polarities together (collective switching) or sequentially (individual switching).[19,21]

To experimentally test our theoretical predictions, we perform a systematic study on $Al_{1-x}Gd_xN$ thin-film capacitors and observe room-temperature ferroelectricity at compositions with $x \geq 0.12$, with E_c decreasing with increasing Gd content, both in agreement with our computational predictions. Our work broadens the palette of functionalities in wurtzite nitrides to include potential multiferroicity and opto-ferroelectricity.[22,23]

II. METHODS

A. Computational

1. DFT parameters

We used Vienna *Ab initio* Simulation Package (VASP 5.4.4) to perform density functional theory (DFT) calculations.[24] All the calculations are based on the following description unless specified. We used plane-wave basis sets with a cutoff kinetic energy of 340 eV and the generalized gradient approximation (GGA) of Perdew–Burke–Ernzerhof (PBE) as the exchange correlation functional.[25] The valence electrons were treated with the projector-augmented wave (PAW) method.[26] In particular, the following pseudopotentials distributed with VASP were utilized: Al 04Jan2001, N_s 07Sep2000, Gd_3 06Sep2000, and B_s 22Jan2003. We applied an effective on-site Hubbard potential U = 3.0 eV to the Sc d orbitals. The Brillouin zone was sampled using an automatically generated Γ-centered Monkhorst–Pack $\boldsymbol{k}$-point grid defined by a length factor (R_k) of 20.

2. Switching barrier

The solid-state nudged elastic band (SS-NEB) method was used to find the polarization switching pathways between the positive- and negative-polarity structures.[27] We utilized the VASP Transition State Theory (VTST) tools developed by Henkelman and Johnson,[28] as implemented in the vtst-182 code. The positive- and negative-polarity structures were fully relaxed (cell volume and shape and ion positions), and we generated the initial images along the pathway via linear interpolation between them. The SS-NEB calculations were iterated until the forces on each atom were below the tolerance of 10^{-2} eV/Å. We note that a large number of intermediate images (>100) are needed to fully resolve the complex minimum energy pathways for the alloys. More details, including guidelines for convergence, can be found in Ref. 21.

3. Polarization

The modern theory of polarization, as implemented in VASP 5.4.4., was applied to calculate the electronic contribution to the spontaneous polarization.[29,30] This approach is based on the Berry phase approximation, and we chose (0.25, 0.25, 0.25) crystal coordinates as the center of the reference frame for dipole calculations. Point charges for the ionic contribution were assumed. Using the SS-NEB pathway, we utilized the implementation in pymatgen to determine smooth adiabatic paths and lattice quanta.[31] We visually inspected the smoothness of the paths and manually identified the smooth ones if the smooth path finding algorithm in pymatgen failed.

4. Electronic bandgap

The hybrid functional HSE06 was utilized to fully relax the 72-atom supercells for AlN-based alloys and to calculate their electronic band structure. The Brillouin zone was sampled using a Γ-centered Monkhorst–Pack 2 × 2 × 2 $\boldsymbol{k}$-point grid. Bandgaps of the alloys were obtained by averaging over four supercells.

5. Born effective charge

We calculated the Born effective charges based on self-consistent response to finite electric field, with the fourth order finite difference stencil, as implemented in VASP. Homogeneous electric fields in the x, y, and z directions are set at 0.01 eV/Å. Damped molecular dynamics method was used to calculate the self-consistent response, and a time step of 0.1 was chosen to ensure convergence. We used a kinetic energy cutoff of 520 eV and Γ-centered Monkhorst–Pack $\boldsymbol{k}$-point grids corresponding to

$n_{kpts} \times n_{atoms} \approx 2000$, where n_{kpts} and n_{atoms} are the numbers of $\boldsymbol{k}$ points and atoms in the cell, respectively.

6. Structural distortion

The wurtzite c/a lattice parameter ratio was calculated to characterize the global structural changes induced by alloying. The c/a ratio is calculated for the fully-relaxed structures, and we only considered the lengths of the lattice vectors a, b, and c, such that

$$c/a = \frac{|c|}{0.5(|a| + |b|)}. \quad (1)$$

The Al–N bond lengths were computed to capture the local structural changes due to alloying. We used the Al–N bond lengths in relaxed wurtzite AlN as the reference. The bonds are categorized into axial and basal-plane bonds based on the direction of the polar axis. Considering the volume change due to alloying, we also scaled the reference bond lengths by $\sqrt[3]{\frac{V_{alloy}}{V_{AlN}}}$, where V_{alloy} and V_{AlN} are volumes of relaxed supercells of AlN-based alloys and wurtzite AlN, respectively. The Al–N bonds in relaxed structures of AlN-based alloys are also categorized into axial and basal-plane bonds. We calculated the deviation from the reference Al–N bond lengths only within the same sets.

B. Experimental

1. Synthesis

The 200–260 nm $Al_{1-x}Gd_xN$ films were deposited on platinized silicon substrates via reactive RF magnetron sputtering under the following growth conditions: 2 mTorr of Ar/N_2 (5/15 sccm flow) and a target power density of 7.4 W/cm^2 on a 2 in. diameter Al target and 0–2.5 W/cm^2 on a 2 in. diameter Gd target. The substrate was rotated and heated to 400 °C during deposition. The base pressure, partial oxygen, and water vapor pressure at 400 °C were $<2 \times 10^{-7}$ Torr, $P_{O_2} < 2 \times 10^{-8}$ Torr, and $P_{H2O} < 1 \times 10^{-7}$ Torr, respectively. Top Au (100 nm)/Ti (20 nm) contacts (50 μm in diameter) were deposited on the $Al_{1-x}Gd_xN$ film via electron beam evaporation through a metal shadow mask pattern.

2. Characterization

The crystal structure of the film is investigated using x-ray diffraction (XRD) on a Bruker D8 DISCOVER diffractometer. The XRD profiles were obtained by integration of 2-dimensional detector images. The c lattice parameter is determined by pseudo-Voigt fitting of the wurtzite (002) diffraction peak assuming a hexagonal lattice. The cation composition is measured using x-ray fluorescence analysis calibrated with microprobe analysis described in our previous study.[32]

Ferroelectric polarization—electric field hysteresis and current—electric field curve measurements were taken with a Precision Multiferroic system from Radiant Technologies. The applied triangle excitation field was up to 6000 kV cm^{-1} at 10 kHz. To wake-up the polarization–electric field hysteresis, we applied the electric field ~5 times sequentially. The remanent polarization, P_r, was calculated from time dependent current under the triangular excitation field, which is expressed as

$$P_r = \frac{1}{2}\int j_s dt = \frac{1}{2}\int (j - j_c - j_l) dt, \quad (2)$$

where j_s is the switching current density, j is the measured current density, j_c is the capacitive current density, and j_l is the leakage current density. The capacitive current density is a positive or negative offset under the triangular electric field determined by the electric field slope and capacitance. The leakage current density is estimated assuming that there is no leakage hysteresis, namely the leakage current density is identical at the same electric field regardless of ramping up or down (Fig. S9).

Magnetic properties were measured via superconducting quantum interference device (SQUID) magnetometry in a Quantum Design Magnetic Property Measurement System (MPMS3) with a vibrating sample magnetometer. The films were measured from T = 2–300 K under applied fields from −7 to +7 T. The measured $Al_{0.86}Gd_{0.14}N$ film was an ~5 × 5 mm^2 piece grown on a p-Si substrate. It was ~230 nm thick. To isolate the signal of the film, a bare substrate was also measured and subtracted.

III. RESULTS AND DISCUSSIONS

A. Predicted ferroelectric parameters of $Al_{1-x}M_x^{3+}N$ alloys

To model $Al_{1-x}M_xN$ (M = Gd, Sc, and B; Sc and B are for benchmarking our computational models) alloys at a given x, we consider four 72-atom supercells ($3 \times 3 \times 2$ of the wurtzite AlN unit cell) with Al randomly substituted with M. Since the alloys are ensembles of different local environments, we consider four different alloy structures for each composition to achieve a balance between ensemble sampling and computational cost. We previously adopted this approach to model polarization switching properties of $Al_{1-x}Sc_xN$ and found good agreement with published experimental results.[21] At each x, we statistically averaged the structural, electronic, and ferroelectric properties across the four supercell models.

Figure 1(b) shows the calculated polarization switching barrier (ω_s) as a function of alloy composition (x) of $Al_{1-x}M_xN$ (M = B, Sc, and Gd). Our previous results for $Al_{1-x}Sc_xN$ alloys are included in Ref. 21 For $Al_{1-x}Sc_xN$, we found that ω_s decreases almost linearly with increasing Sc content, which is qualitatively consistent with the reported linear decrease in experimental E_c with x.[10,14,21,33] More importantly, we found that the polarization switching process at the atomic scale depends on the alloy composition. At low x, collective switching prevails, in which the cation and anion sublattices *collectively* squeeze through one another via a nonpolar hexagonal BN-like structure. Collective switching essentially causes *all* cation-centered tetrahedra to "flip" simultaneously along the polar axis, e.g., from pointing along c to $-c$. At larger Sc compositions ($x \gtrsim 0.28$), "individual" switching is observed, in which the cation-centered tetrahedra flip along the polar axis in a sequential manner rather than collectively. The collective and individual mechanisms are discussed in more detail in Ref. 21. Of particular importance to this work is the observation that when individual switching is observed, it represents a lower energy barrier to polarization reversal than the corresponding collective switching pathway.

For benchmarking, we calculated the polarization switching properties, including ω_s and spontaneous polarization (P_s), of $Al_{1-x}B_xN$ alloys (Fig. 1). The transition from collective to individual switching mechanism with increasing B composition is similar to that found in $Al_{1-x}Sc_xN$. At low B compositions (e.g., x = 0.028),

collective switching is observed in all four alloy supercells. Interestingly, ω_s increases slightly relative to AlN, which is attributed to the slightly larger kinetic barrier near the peak of the minimum energy pathway associated with moving B across the hexagonal BN plane (Fig. S1). With further increase in B composition beyond $x = 0.055$, individual switching is observed in all four alloy supercells along with a concomitant decrease in ω_s, again similar to $Al_{1-x}Sc_xN$.[21] In contrast, the transition in the switching mechanism occurs at much lower B compositions ($x \sim 0.055$) compared to $Al_{1-x}Sc_xN$ ($x \sim 0.28$). Beyond $x = 0.055$, ω_s plateaus, unlike in $Al_{1-x}Sc_xN$, where ω_s progressively decreases almost linearly up to $x = 0.44$ (highest x considered). Our computational results are qualitatively in agreement with the experimental report by Hayden *et al.*,[12] in which the authors demonstrated ferroelectric behavior at $x \gtrsim 0.02$ and plateauing of the coercive field at $x \gtrsim 0.13$. However, we must note that even though we predicted lower ω_s for $Al_{1-x}B_xN$ compared to $Al_{1-x}Sc_xN$, experimentally measured coercive fields in ferroelectric $Al_{1-x}B_xN$ thin films are higher than in $Al_{1-x}Sc_xN$. It is known that experimental coercive fields are dominated by extrinsic factors, such as measurement frequency,[34] defects,[35,36] and domain wall structure,[37,38] which are not taken into account in the DFT calculations. Future studies should address larger length-scale simulations that account for domain walls, as has been done for oxide perovskites.[39]

We find that AlN alloyed with Gd exhibits a similar polarization switching behavior to alloys with Sc and B. Similar to B, alloying with Gd induces a slight increase in ω_s at $x = 0.028$ followed by a drop in ω_s at $x = 0.055$, which is associated with the transition from the collective to individual switching mechanism. However, there are subtle differences in the trends seen for B and Gd. For Gd, the initial increase in ω_s at $x = 0.028$ and drop at $x = 0.55$ are less abrupt compared to B. Unlike B, Gd alloying does not induce a sudden transition from collective to individual switching, but instead, there is a transition region where collective switching is observed in some supercells, while individual switching is seen in others, similar to $Al_{1-x}Sc_xN$.[21] While the limited number of supercells and finite compositions studied demand caution, the results suggest that B is more effective in promoting individual switching than Gd or Sc. From these results and comparisons with $Al_{1-x}Sc_xN$, we predict that room temperature ferroelectric switching should be feasible in wurtzite $Al_{1-x}Gd_xN$ for $x \geq 0.14$.

Next, we assess the effect of alloying on spontaneous polarization (P_s). The calculated P_s decreases with increasing Sc and Gd content (x), while it increases with B content in $Al_{1-x}M_xN$ alloys [Fig. 1(d)]. The latter is consistent with previously reported calculations.[12,40] At first glance, the P_s increase with B content is unintuitive because the addition of B introduces large structural distortions away from the perfect wurtzite crystal structure of AlN; such distortions generally lead to lowering of P_s based on our current understanding of $Al_{1-x}Sc_xN$ alloys and the resulting reduction in the wurtzite c/a lattice parameter ratio [Fig. 1(e)]. However, P_s also inversely depends on cell volume. Owing to the small size of B, alloying causes a sharp decrease in the cell volume (by ~6.2% at $x = 0.14$), as shown in Fig. S4. Therefore, the increase in P_s is due to the volume contraction associated with B alloying. Alloying with Sc and Gd is associated with a quantitatively similar and almost linear decrease in P_s with increasing x [Fig. 1(e)].

A side effect of alloying AlN with M = Sc and Gd is the reduction in the bandgap because these MN nitrides are either metallic or small bandgap rocksalts.[41–43] h-BN has a hexagonal structure with a large indirect bandgap of 5.9 eV.[44] Bandgap reduction can reduce the breakdown field and/or increase leakage currents—both undesirable for dielectrics. We calculated the bandgaps of $Al_{1-x}M_xN$ for a limited range of compositions using the hybrid DFT functional HSE06 (see Fig. S3) and found that the calculated average bandgap of $Al_{0.86}Gd_{0.14}N$ (~4.5 eV) is comparable to that of $Al_{0.64}Sc_{0.36}N$ (~4.6 eV). Therefore, relatively large bandgaps are maintained upon alloying AlN with Gd within the range of compositions explored in this study.

Since a transition in the switching mechanism from collective to individual switching is associated with a substantial reduction in the switching barrier and is, thus, a promising strategy for reducing E_c below breakdown field, we seek to deduce the underlying composition–structure–property relationships.[19,21] There is emerging evidence that larger structural distortions away from the ideal wurtzite crystal structure promote polarization switching.[19] Given the large differences in the ionic radii between Al and M = B, Sc, and Gd, we quantitatively investigate the local structural distortions in $Al_{1-x}M_xN$ alloys. Figure 1(c) shows the distribution of deviations in Al–N bond length in $Al_{0.945}M_{0.055}N$ relative to pristine AlN of the same volume (see Sec. II for details). We categorize the bond length deviations into basal and axial Al–N bonds; the cumulative probability of the basal bond length deviation is higher than that of the axial bonds because the number of basal bonds is three times that of the axial bonds. The shape of the distribution is an indicator of the extent of the distortion. Small distortions will translate to tight distributions with a single strong peak near zero deviation, while larger distortions will result in wider and flatter distributions. The distributions of basal Al–N bond length deviations are characterized by multiple peaks (bimodal and trimodal distributions), while the distributions of the axial bonds are more gradual, regardless of M. The deviations in the Al–N bond lengths reflect changes in the local structure in the vicinity of M. The Al–N bonds in the vicinity of B, where Al and B form bonds with the same N, are relatively longer than the average Al–N bonds in AlN. The opposite is the case of Sc and Gd, where those Al–N bonds are relatively shorter. The difference in the behavior between B and Gd/Sc is related to the M–N bond lengths in their respective ground-state structures, with B–N bond lengths in hexagonal BN being significantly shorter than Sc–N and Gd–N bond lengths in the rocksalt structures. Among the three M considered, Gd alloying induces the largest structural distortions compared to Sc and B, while still maintaining tetrahedral coordination of Gd up to $x = 0.22$.

In our previous studies,[14,19,21] we have proposed that the increased ionicity of Sc–N bonds (relative to Al–N) promotes polarization switching in $Al_{1-x}Sc_xN$. M are nominally 3+ cations, but M–N have both ionic and covalent character. Born effective charge is one indicator of the degree of iono-covalency of the bonds, but it also accounts for the lattice softness.[14] Fig. 1(f) shows the Born effective charges along the polar c axis as a function of the alloy composition. The Born effective charges in the a–b plane are shown in Fig. S5. Gd has the highest Born effective charges followed by Sc, Al, and B, which are consistent with their Pauling electronegativities. Alloying does not considerably affect the average Born effective charges of Al,

but the standard deviation increases, reflecting the local structural distortions (Fig. S5).

B. Experimental verification of ferroelectricity in $Al_{1-x}Gd_xN$ alloys

To investigate the predicted ferroelectricity of Gd-substituted AlN, we deposited $Al_{1-x}Gd_xN$ thin films of various compositions (x) on platinized silicon substrates to fabricate ferroelectric capacitors (see Sec. II). The $Al_{1-x}Gd_xN$ films crystallize in a phase-pure wurtzite structure up to at least $x = 0.18$, with strong polar-axis texture up to $x = 0.14$ [Fig. 2(a)]. The diffraction patterns show wurtzite diffraction peaks originating from the $Al_{1-x}Gd_xN$ films as well as a (111) peak from the Pt bottom electrode. Successful incorporation of Gd in AlN is confirmed by the increase in the lattice parameter with Gd content [Fig. 2(b)]. The lattice parameter c is in good agreement with our previous report on $Al_{1-x}Gd_xN$ films on Si substrates,[32] and the trend is consistent with our DFT results (Fig. S4). The detailed lattice parameter analysis and microstructure on $Al_{1-x}Gd_xN$ films were discussed in the previous report.[32]

The (100) and (101) wurtzite diffraction peaks observed in the film with $x = 0.18$ indicate various out-of-plane crystal orientations, whose polar axes are not parallel to the surface normal direction and extrinsically affect the observed ferroelectric properties. The omega rocking curves for the (002) diffraction peak for the film with $x = 0.18$ is broad and poorly textured compared to the films with $x \leq 0.14$, which are consistent with the 2 theta profiles [Fig. 2(c)]. The full width at half maximum (FWHM) of the rocking curve ranges from 2° to 4° for the textured films with an increasing trend with Gd content, while the film with $x = 0.18$ has ~9° FWHM [Fig. 2(d)]. Hereafter, we focus on the films with $x \leq 0.14$ for the ferroelectric measurements.

Unambiguous ferroelectric hysteresis loops are observed for the $Al_{1-x}Gd_xN$ films. As shown in Fig. 3(a), the nested ferroelectric polarization–electric field loops of $Al_{0.88}Gd_{0.12}N$ taken at 190 °C are square and possess a large remanent polarization (>100 μC cm^{-2}), comparable to other wurtzite AlN-based ferroelectrics.[10,45] Along with the hysteresis loops, distinct switching current peaks at the coercive field (~4000 kV cm^{-1}) are observed, supporting the polarization reorientation under the electric field. The ferroelectric switching between the two distinct up- and down-polar states is confirmed with the abrupt increase in remanent polarization at the coercive field and remanent polarization saturation beyond the coercive field, as shown in Fig. 3(b). The gradual increase in the polarization is associated with the leakage current contribution, which complicates the quantification of the precise remanent polarization value from the plot.

To understand the effects of Gd substitution and compare the experiments to the computational predictions, we investigated the ferroelectric properties as a function of composition. Figure 4(a) illustrates the coercive field contour map for various x and measurement temperatures, based on hysteresis loops in the variable space (Fig. S6). At room temperature, the films with $x \geq 0.12$ show ferroelectric switching, which is quantitatively consistent with the computational prediction showing an abrupt switching barrier decrease at $x \approx 0.14$ [Fig. 1(b)]. At room temperature, the films with $x < 0.12$ do not show ferroelectric switching and undergo dielectric breakdown at an electric field that is lower than the coercive field. The

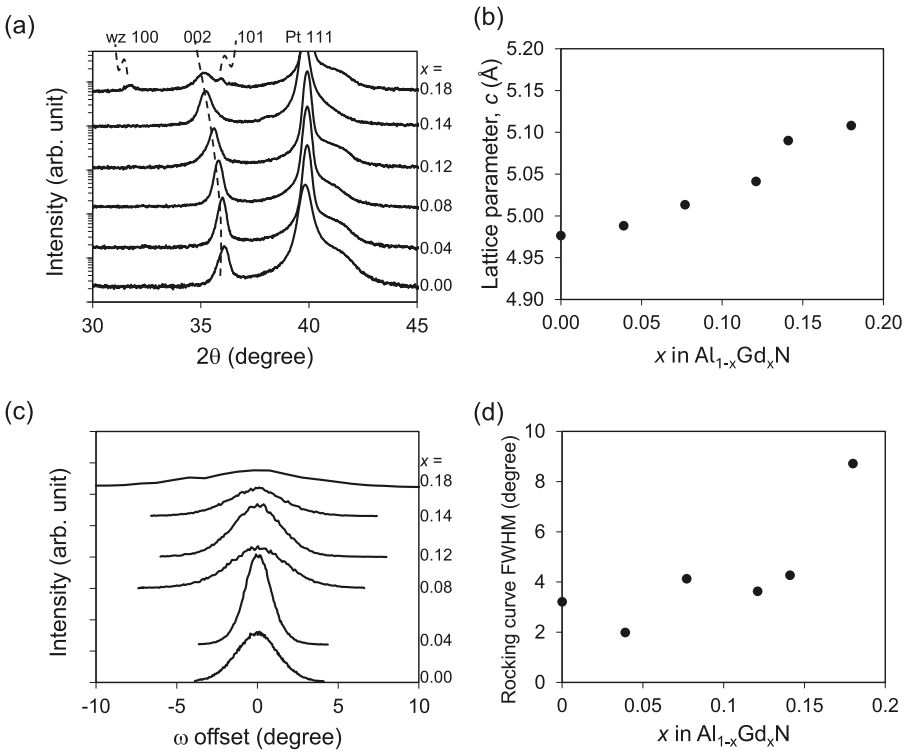

FIG. 2. Crystal structure of $Al_{1-x}Gd_xN$ films on $Pt/TiO_2/SiO_2/Si$ substrate. (a) XRD 2θ profiles shows pure wurtzite phase and polar texture up to $x = 0.14$. (b) Lattice parameter increases with Gd content, indicating a solid solution. (c) XRD rocking curves of wurtzite (002) diffraction peaks, and (d) the full width at half maximum (FWHM) of rocking curves show degradation of wurtzite (001) texturing for the film with $x = 0.18$.

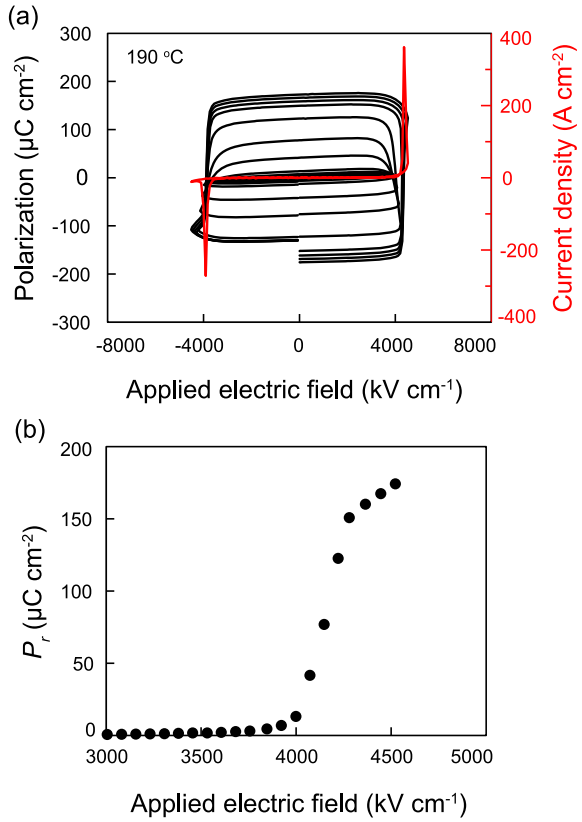

FIG. 3. Ferroelectric hysteresis loops for $Al_{0.88}Gd_{0.12}N$ at 190 °C. (a) Nested polarization–electric field hysteresis and current loops show ferroelectric switching. (b) Saturation behavior of remanent polarization (P_r).

switchable composition range widens with increased measurement temperature. Above 140 °C, polarization switching is observed for values as low as $x = 0.03$. In addition, the coercive field decreases with increased measurement temperature, which is consistent with other wurtzite FEs.[12,13,46,47]

The coercive field also decreases with increased Gd content. Figure 4(b) shows the extracted coercive fields and breakdown fields under ferroelectric loop measurement conditions (10 kHz bipolar triangular voltage) as a function of Gd content at 190 °C. The trend of decreasing coercive field is consistent with the calculated barrier height [Fig. 1(b)]. Note that the absolute value of the experimental coercive field is not directly transferable from the barrier height due to extrinsic effects such as defects and domain structures.[35–38]

The relationship between the coercive field and (greater) breakdown field enables ferroelectric switching. In the current study, the breakdown field does not change substantially with Gd content, although there are large error bars attributed to the inter-device variability (~ ±400 kV cm^{-1}). Extrapolating coercive field from this study to a composition of $x = 0$ suggests a value of ~5000 kV cm^{-1}, which is comparable to both the breakdown strength for all samples in the current study and the reported coercive field of AlN at 190 °C.[47] Thus, the low-temperature and low-Gd content region of

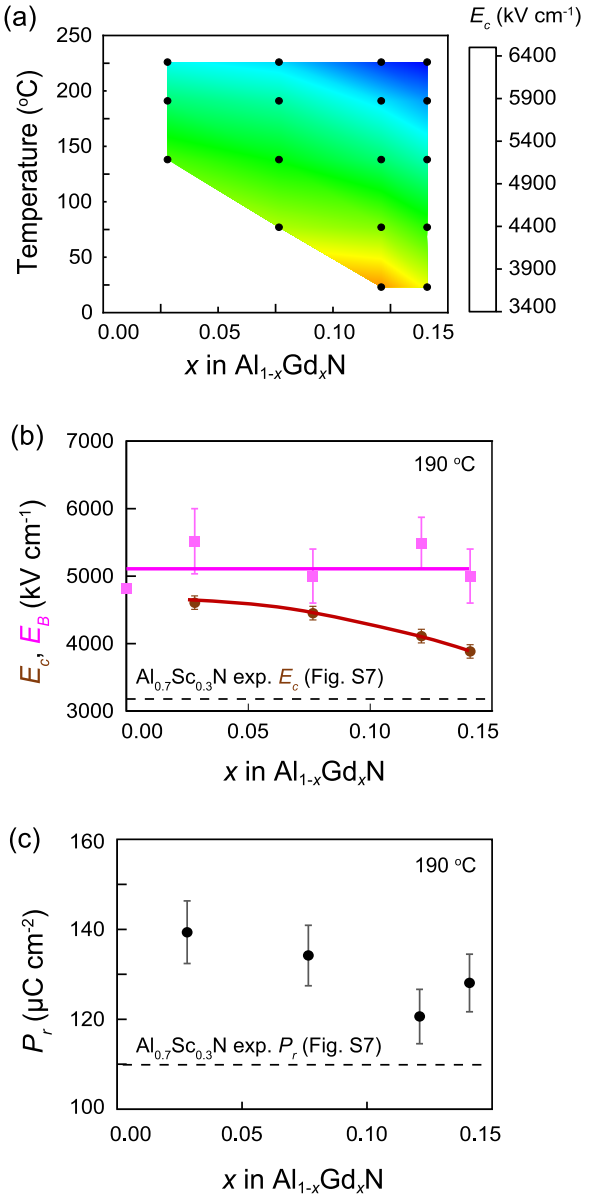

FIG. 4. Ferroelectric properties of $Al_{1-x}Gd_xN$ in composition and measurement temperature space. (a) Coercive field contour map in ferroelectric switchable range. The black dots represent measurement points, and the color map is linearly interpolated. (b) Coercive field and breakdown field as a function of Gd content at 190 °C, showing that the coercive field decreases with Gd content, while the breakdown field does not change substantially. (c) Remanent polarization decreases with Gd content. For comparison, the coercive field of an $Al_{0.7}Sc_{0.3}N$ film under the same measurement condition (Fig. S7, supplementary material) is shown as a horizontal dashed line.

Fig. 4(a), where switching is not observed, is explained by the coercive field increasing beyond the breakdown field. This relationship and its temperature-dependence are shown further in Fig. S8 of the supplementary material.

Remanent polarization also decreases with Gd content. The remanent polarization values are obtained by removing leakage and capacitive contributions from switching current measurements (see Sec. II and Fig. S9 of the supplementary material).[48] Figure 4(c) shows the extracted remanent polarization as a function of Gd content at 190 °C. The uncertainty is dominated by uncertainty in defining the electrode boundary and, thus, device size, but the trend is comparable to the DFT calculations [Fig. 1(e)].

We note that $Al_{1-x}Gd_xN$ is the first example of an AlN-based ferroelectric material that incorporates a magnetic rare-earth cation and, thus, might exhibit interesting magnetic properties. To test whether the addition of magnetic (Gd^{3+}) to AlN might induce magnetic order and thus multiferroicity, we measured the magnetic susceptibility of an $Al_{0.86}Gd_{0.14}N$ film grown on a Si substrate. As shown in Fig. S10, no evidence of long-range magnetic ordering was observed down to $T = 2$ K. The magnetization as a function of applied magnetic field exhibits no hysteresis curve at $T = 2$ K, and no peak is observed as a function of temperature: the data are consistent with paramagnetism and Gd^{3+} cations. Some of the primary challenges of introducing multiferroicity to this family of materials will be (1) introducing a sufficient amount of the magnetic cation to induce long-range magnetic order and that (2) the tetrahedral coordination may often lead to antiferromagnetic interactions instead of ferromagnetic interactions, which are more technologically useful. However, single-phase multiferroics are exceedingly rare, so if this family of materials can successfully be designed to simultaneously exhibit ferroelectricity and magnetic order (i.e., by incorporating enough of a magnetic cation), it will not only be scientifically interesting (as these properties are generally mutually exclusive) but also highly relevant to applications in energy technologies such as spintronics and low-power computing.

IV. CONCLUSION

In summary, we computationally predict and experimentally verify ferroelectricity at room temperature in $Al_{1-x}Gd_xN$ alloys. Our calculations show that $Al_{1-x}Gd_xN$, along with $Al_{1-x}B_xN$, have a drastic change in the polarization switching barrier due to a change in switching mechanisms as the amount of alloying element is increased. Further structural analysis shows that larger local distortions due to alloying promote this change in the switching mechanism from collective to individual. Our predictions for the alloy compositions, where this change in switching mechanisms occurs for $Al_{1-x}B_xN$ and $Al_{1-x}Gd_xN$, are qualitatively consistent with experimental results, with ferroelectric switching clearly demonstrated at low alloying contents ($x \lesssim 0.1$). These results provide strong evidence that promoting individual switching at the atomic scale can assist with ferroelectric switching in wurtzite AlN-based alloys by reducing coercive fields. We note, however, that the predicted intrinsic switching barriers are not yet quantitatively comparable to experimentally measured coercive field values. Finally, the $Al_{1-x}Gd_xN$ alloy is the first experimentally demonstrated wurtzite ferroelectric material with a rare-earth cation. This suggests a route to possible multi-functionality, such as multiferroicity and opto-ferroicity in tetrahedral-based microelectronics.

SUPPLEMENTARY MATERIAL

See the supplementary material for the details in the minimum energy paths for $Al_{0.972}M_{0.028}N$ alloys (M = Sc, B, and Gd), hybrid DFT functional HSE06 bandgap, the standard deviation for Figs. 1(b), 1(d), 1(e), and 1(f), predicted structural data of $Al_{1-x}M_xN$ alloys (M = Sc, B, Gd), measured ferroelectric hysteresis loops for $Al_{1-x}Gd_xN$ films with various Gd contents and temperatures, breakdown field and coercive field comparison at 23, 75, 140, and 225 °C, time dependence of measured current for remanent polarization calculation, and magnetic susceptibility measurements on the $Al_{0.86}Gd_{0.14}N$ film grown on a pSi substrate.

ACKNOWLEDGMENTS

This work was authored in part by the National Renewable Energy Laboratory, operated by Alliance for Sustainable Energy, LLC, for the U.S. Department of Energy (DOE) under Contract No. DE-AC36-08GO28308. Funding provided by the Department of Energy, Office of Science, Basic Energy Sciences, Division of Materials Sciences through laboratory program Announcement No. LAB 21-2491: Microelectronics Co-Design Research, with additional support from Advanced Scientific Computing Research (ASCR), under Program No. ERW6548 (DFT calculations and film growths) and the Laboratory Directed Research and Development (LDRD) Program at NREL (XRD and magnetism data analysis). The work was also supported by the National Science Foundation under Grant No. DMR-2119281 (Ferroelectric characterization). This work used computational resources sponsored by the Department of Energy's Office of Energy Efficiency and Renewable Energy, located at NREL. The magnetic measurements were supported by the U.S. Department of Energy, Office of Science, Basic Energy Sciences, Division of Materials Sciences through Funding Opportunity Announcement (FOA) No. DE-FOA-0002676: Chemical and Materials Sciences to Advance Clean-Energy Technologies and Transform Manufacturing (magnetic measurements). The authors acknowledge the Analytical Resources Core (RRID: SCR_021758) at Colorado State University for instrument access, training, and assistance with sample analysis. The authors also express their appreciation to Dr. Andriy Zakutayev for feedback to an early version of this article. The views expressed in the article do not necessarily represent the views of the DOE or the U.S. Government.

AUTHOR DECLARATIONS

Conflict of Interest

The authors have no conflicts to disclose.

Author Contributions

Cheng-Wei Lee: Data curation (equal); Investigation (equal); Writing – original draft (equal). **Rebecca W. Smaha**: Investigation (supporting); Writing – review & editing (equal). **Geoff L. Brennecka**: Funding acquisition (equal); Project administration (equal); Supervision (supporting); Writing – review & editing (equal).

Nancy M. Haegel: Funding acquisition (equal); Project administration (equal); Supervision (supporting); Writing – review & editing (equal). **Prashun Gorai**: Conceptualization (supporting); Data curation (equal); Investigation (supporting); Supervision (lead); Writing – review & editing (equal). **Keisuke Yazawa**: Conceptualization (lead); Data curation (equal); Formal analysis (equal); Investigation (equal); Supervision (supporting); Visualization (equal); Writing – original draft (equal); Writing – review & editing (equal).

DATA AVAILABILITY

Data associated with this study are available from the corresponding author upon request. See Ref. 49 for the SS-NEB polarization pathways and the associated structures.

REFERENCES

[1] D. Ielmini and H. S. Wong, Nat. Electron. **1**, 333 (2018).
[2] S. Oh, H. Hwang, and I. K. Yoo, APL Mater. **7**, 091109 (2019).
[3] K.-H. Kim, I. Karpov, R. H. Olsson, and D. Jariwala, Nat. Nanotechnol. **18**, 422 (2023).
[4] O. Ambacher, F. Freudenberg, R. Dimitrov, H. Angerer, and M. Stutzmann, Jpn. J. Appl. Phys. **37**, 2416 (1998).
[5] M. Sterntzke and G. Müller, J. Am. Ceram. Soc. **77**, 737 (1994).
[6] S. Mueller, J. Müller, U. Schroeder, and T. Mikolajick, IEEE Trans. Device Mater. Reliab. **13**, 93 (2013).
[7] S. J. Yoon, D. H. Min, S. E. Moon, K. S. Park, J. I. Won, and S. M. Yoon, IEEE Trans. Electron Devices **67**, 499 (2020).
[8] J. Breternitz and S. Schorr, Acta Crystallogr., Sect. A: Found. Adv. **77**, 208 (2021).
[9] C.-W. Lee, N. U. Din, G. L. Brennecka, and P. Gorai, Appl. Phys. Lett. **125**, 022901 (2024).
[10] S. Fichtner, N. Wolff, F. Lofink, L. Kienle, and B. Wagner, J. Appl. Phys. **125**, 114103 (2019).
[11] D. Wang, P. Wang, B. Wang, and Z. Mi, Appl. Phys. Lett. **119**, 111902 (2021).
[12] J. Hayden, M. D. Hossain, Y. Xiong, K. Ferri, W. Zhu, M. V. Imperatore, N. Giebink, S. Trolier-McKinstry, I. Dabo, and J.-P. Maria, Phys. Rev. Mater. **5**, 044412 (2021).
[13] K. Ferri, S. Bachu, W. Zhu, M. Imperatore, J. Hayden, N. Alem, N. Giebink, S. Trolier-McKinstry, and J.-P. Maria, J. Appl. Phys. **130**, 044101 (2021).
[14] K. Yazawa, J. S. Mangum, P. Gorai, G. L. Brennecka, and A. Zakutayev, J. Mater. Chem. C **10**, 17557 (2022).
[15] K. Yazawa, A. Zakutayev, and G. L. Brennecka, Appl. Phys. Lett. **121**, 042902 (2022).
[16] H. Moriwake, A. Konishi, T. Ogawa, K. Fujimura, C. A. Fisher, A. Kuwabara, T. Shimizu, S. Yasui, and M. Itoh, Appl. Phys. Lett. **104**, 242909 (2014).
[17] H. Moriwake, R. Yokoi, A. Taguchi, T. Ogawa, C. A. J. Fisher, A. Kuwabara, Y. Sato, T. Shimizu, Y. Hamasaki, H. Takashima, and M. Itoh, APL Mater. **8**, 121102 (2020).
[18] Y. Dai and M. Wu, Sci. Adv. **9**, eadf8706 (2023).
[19] C. W. Lee, N. U. Din, K. Yazawa, G. L. Brennecka, A. Zakutayev, and P. Gorai, Matter **7**, 1644 (2024).
[20] D. Wang, S. Mondal, J. Liu, M. Hu, P. Wang, S. Yang, D. Wang, Y. Xiao, Y. Wu, T. Ma, and Z. Mi, Appl. Phys. Lett. **123**, 033504 (2023).
[21] C.-W. Lee, K. Yazawa, A. Zakutayev, G. L. Brennecka, and P. Gorai, Sci. Adv. **10**, eadl0848 (2024).
[22] J. Hao, Y. Zhang, and X. Wei, Angew. Chem., Int. Ed. **50**, 6876 (2011).
[23] Y. Zhang, W. Jie, P. Chen, W. Liu, J. Hao, Y. Zhang, P. Chen, W. Liu, W. Jie, and J. Hao, Adv. Mater. **30**, 1707007 (2018).
[24] G. Kresse and J. Furthmüller, Phys. Rev. B **54**, 11169 (1996).
[25] J. P. Perdew, K. Burke, and M. Ernzerhof, Phys. Rev. Lett. **77**, 3865 (1996).
[26] G. Kresse and D. Joubert, Phys. Rev. B **59**, 1758 (1999).
[27] D. Sheppard, P. Xiao, W. Chemelewski, D. D. Johnson, and G. Henkelman, J. Chem. Phys. **136**, 074103 (2012).
[28] G. Henkelman, B. P. Uberuaga, and H. Jónsson, J. Chem. Phys. **113**, 9901 (2000).
[29] R. D. King-Smith and D. Vanderbilt, Phys. Rev. B **47**, 1651 (1993).
[30] R. Resta, Rev. Mod. Phys. **66**, 899 (1994).
[31] T. E. Smidt, S. A. Mack, S. E. Reyes-Lillo, A. Jain, and J. B. Neaton, Sci. Data **7**, 72 (2020).
[32] R. W. Smaha, K. Yazawa, A. G. Norman, J. S. Mangum, H. Guthrey, G. L. Brennecka, A. Zakutayev, S. R. Bauers, P. Gorai, and N. M. Haegel, Chem. Mater. **34**, 10639 (2022).
[33] S. Yasuoka, T. Shimizu, A. Tateyama, M. Uehara, H. Yamada, M. Akiyama, Y. Hiranaga, Y. Cho, and H. Funakubo, J. Appl. Phys. **128**, 114103 (2020).
[34] J. F. Scott, Integr. Ferroelectr. **12**, 71 (1996).
[35] K. Kitamura, Y. Furukawa, K. Niwa, V. Gopalan, and T. E. Mitchell, Appl. Phys. Lett. **73**, 3073 (1998).
[36] S. Kim, V. Gopalan, and A. Gruverman, Appl. Phys. Lett. **80**, 2740 (2002).
[37] S. Choudhury, Y. Li, N. Odagawa, A. Vasudevarao, L. Tian, P. Capek, V. Dierolf, A. N. Morozovska, E. A. Eliseev, S. Kalinin, Y. Cho, L. Q. Chen, and V. Gopalan, J. Appl. Phys. **104**, 084107 (2008).
[38] K. Yazawa, H. Uchida, and J. E. Blendell, Adv. Funct. Mater. **30**, 1909100 (2020).
[39] Y.-H. Shin, I. Grinberg, I.-W. Chen, and A. M. Rappe, Nature **449**, 881 (2007).
[40] Z. Liu, X. Wang, X. Ma, Y. Yang, and D. Wu, Appl. Phys. Lett. **122**, 122901 (2023).
[41] H. J. Trodahl, A. R. H. Preston, J. Zhong, B. J. Ruck, N. M. Strickland, C. Mitra, and W. R. L. Lambrecht, Phys. Rev. B **76**, 085211 (2007).
[42] P. Wachter, Adv. Mater. Phys. Chem. **6**, 28 (2016).
[43] Z. Deng and E. Kioupakis, AIP Adv. **11**, 065312 (2021).
[44] G. Cassabois, P. Valvin, and B. Gil, Nat. Photonics **10**, 262 (2016).
[45] K. Yazawa, D. Drury, A. Zakutayev, and G. L. Brennecka, Appl. Phys. Lett. **118**, 162903 (2021).
[46] D. Drury, K. Yazawa, A. Zakutayev, B. Hanrahan, and G. Brennecka, Micromachines **13**, 887 (2022).
[47] W. Zhu, J. Hayden, F. He, J.-I. Yang, P. Tipsawat, M. D. Hossain, J.-P. Maria, and S. Trolier-McKinstry, Appl. Phys. Lett. **119**, 062901 (2021).
[48] K. Yazawa, B. Ducharne, H. Uchida, H. Funakubo, and J. E. Blendell, Appl. Phys. Lett. **117**, 012902 (2020).
[49] P. Gorai and C.-W. Lee (2025). "Supporting information," GitHub. https://github.com/prashungorai/papers/tree/main/2025/almn-alloys-polarization-switching